Optical reflectivity and hardness improvement of hafnium nitride films via tantalum alloying

Zhiqing Gu, Haihua Huang, Sam Zhang, Xiaoyi Wang, Jing Gao, Lei Zhao, Weitao Zheng, and Chaoquan Hu

Articles you may be interested in

Improved interface properties of GaN metal-oxide-semiconductor device with non-polar plane and AlN passivation layer
Appl. Phys. Lett. **109**, 232101232101 (2016); 10.1063/1.4971352

Tunable whispering gallery modes lasing in dye-doped cholesteric liquid crystal microdroplets
Appl. Phys. Lett. **109**, 231906231906 (2016); 10.1063/1.4971973

III-Nitride-on-silicon microdisk lasers from the blue to the deep ultra-violet
Appl. Phys. Lett. **109**, 231101231101 (2016); 10.1063/1.4971357

Thermal rectification in inhomogeneous nanotubes
Appl. Phys. Lett. **109**, 231905231905 (2016); 10.1063/1.4971390

Optical reflectivity and hardness improvement of hafnium nitride films via tantalum alloying

Zhiqing Gu,[1] Haihua Huang,[1] Sam Zhang,[2] Xiaoyi Wang,[3] Jing Gao,[1] Lei Zhao,[1] Weitao Zheng,[1,4,a)] and Chaoquan Hu[1,a)]

[1]*School of Materials Science and Engineering, State Key Laboratory of Superhard Materials, and Key Laboratory of Automobile Materials of MOE, Jilin University, Changchun 130012, China*
[2]*School of Mechanical and Aerospace Engineering, Nanyang Technological University, 50 Nanyang Avenue, Singapore 639798, Singapore*
[3]*Key Laboratory of Optical System Advanced Manufacturing Technology, Changchun Institute of Optics, Fine Mechanics and Physics, Chinese Academy of Sciences, Changchun 130033, China*
[4]*State Key Laboratory of Automotive Simulation and Control, Jilin University, Changchun 130025, China*

It is found that incorporation of tantalum in a hafnium nitride film induces a tunable optical reflectivity and improves the hardness. The underlying mechanism can be illustrated by a combination of experiments and first-principles calculations. It is shown that the evolution of optical reflectivity and the increase in hardness arise from the formation of $Hf_{1-x}Ta_xN$ solid solutions and the resulting changes in the electronic structure. The increase in infrared reflectance originates from the increase in concentration of free electrons (n) because Ta (d^3s^2) has one more valence electron than Hf (d^2s^2). The sharp blue-shift in cutoff wavelength is attributed to the increase in n and the appearance of $t_{2g} \rightarrow e_g$ interband absorption. These results suggest that alloying of a second transition metal renders an effective avenue to improve simultaneously the optical and mechanical properties of transition metal nitride films. This opens up a door in preparing high-reflectance yet hard films. *Published by AIP Publishing.* [http://dx.doi.org/10.1063/1.4971356]

The Group-*IVB*, *VB*, and *VIB* transition metal nitrides (*TM*N, *TM* = Ti, Zr, Hf, V, Nb, Ta, Cr, Mo, and W) are well known as a class of technologically important materials in the fields of cutting- and machining-tool industries and microelectronic devices.[1–4] Recently, they have attracted much attention because of their gold-like colors[5] and metal-like reflectivity spectra[6] coupled with other properties such as high hardness,[7,8] thermal stability,[9,10] corrosion resistance,[11,12] abrasion resistance,[13,14] oxidation resistance,[15,16] electrical conductivity,[17,18] and good diffusion barrier.[19,20] These make them very promising candidates for applications in reflectors for high-power light-emitting-diode (LED) operation at elevated temperatures,[21] highly reflecting back-contacts in solar cells,[22,23] solar control coatings on windows,[24] scratch-resistant decorative coating,[25–27] selective surface in thermal solar absorbers,[28] and refractory plasmonic materials.[29,30] In these applications, the cutoff wavelength and infrared reflectance of *TM*N films are of utmost importance, as they determine the light utilization and optical selectivity. It is very crucial, therefore, to understand how to control them.

To date, studies on optical reflectivity properties of TiN,[31] ZrN,[32] HfN,[6,33,34] and VN[35] films show that the nitrogen content,[33,35] substrate temperature,[6,35] substrate bias,[32] and thickness[34] exert significant influences on the cutoff wavelength and infrared reflectance, owing to the changes in the microstructure and electronic properties. In addition, the effect of deposition conditions and nitrogen composition on the structure[36] and mechanical properties[37–39] of *TM*N films has also been reported. Although the effect of chemical composition and deposition conditions on reflectivity characteristics has been studied and important results have been reported, how to control the cutoff wavelength and infrared reflectance, and how to enhance the hardness of *TM*N films have not yet been well explored.

In this letter, we report that incorporation of tantalum in the hafnium nitride film induces a tunable optical reflectivity and improves the hardness. The mechanisms on optical evolution and mechanical improvement are revealed by combining the first-principles calculations and Drude-Lorentz fitting with a series of experiments: gracing incident X-ray diffraction (XRD), Raman spectra, selected area electron diffraction (SAED), and high resolution transmission electron microscopy.

The δ-$Hf_{1-x}Ta_xN$ films with a thickness of ~600 nm were prepared by radio-frequency reactive co-sputtering from separate Hf and Ta targets in the mixed discharge gases of Ar and N_2. The distance between the target and substrate holder, working pressure, negative substrate bias, and temperature were fixed at 70 mm, 1.0 Pa, −160 V, and 200 °C, respectively. The Ta content x [Ta/(Ta + Hf)] in the δ-$Hf_{1-x}Ta_xN$ films was modulated from 0 to 0.26 by increasing the power of the Ta target from 0 to 150 W while the power of the Hf target and flow rate of N_2/Ar were kept at 150 W and 2.0/80 sccm, respectively. The pure δ-TaN (Ta/N = 1) film was obtained by keeping RF power of Ta targets and flow rate of N_2/Ar at 150 W and 9.6/80 sccm, respectively. The microstructure of the films was characterized using the X-ray diffraction (XRD), Raman spectra, selected area electron diffraction (SAED), and high-resolution transmission electron microscope (HRTEM). X-ray photoelectron spectroscopy (XPS) was used for measurements of Ta content

a)Authors to whom correspondence should be addressed. Electronic addresses: wtzheng@jlu.edu.cn and cqhu@jlu.edu.cn

x and valence-band spectra, ultraviolet–visible–near-infrared (UV–VIS–NIR) spectrometer and Hall-effect (HL5550) testing equipment for characterization of reflectivity spectra and concentration of free electrons, and Nano indentation and Dektak[3] surface profile for characterization of hardness and thicknesses. Density functional theory (DFT) calculations were performed to explore the electronic structure of the δ-Hf$_{1-x}$Ta$_x$N solid solutions. The details of preparation, characterization, Drude–Lorentz fitting, and computation methods were reported elsewhere.[33,40]

Fig. 1(a) plots the reflectance spectra of Hf$_{1-x}$Ta$_x$N films at different x, wherein there is a cutoff wavelength (λ_{Rmin}) corresponding to a distinct minimum of reflectance in the region of visible to ultraviolet wavelengths. Above λ_{Rmin}, the reflectance rises sharply and then remains a high and almost wavelength-independent constant in the infrared range. Below λ_{Rmin}, the reflectance increases slightly up to an intermediate value in the ultraviolet wavelengths (UV). All reflectance curves exhibit high reflectance in the region from visible to far infrared. λ_{Rmin} is an important factor in evaluating reflectivity characteristic, because low λ_{Rmin} means a broad wavelength range of high reflectance. Figs. 1(b) and 1(c) display the λ_{Rmin} and average reflectance in the infrared wavelength range of 1000–2200 nm (R_{IR}) as a function of x. As x increases from 0 to 1 (Fig. 1(b)), the λ_{Rmin} exhibits a continuous blue-shift from 376 to 244 nm (decrease by 35%). The R_{IR} rises from 77% to a maximum value of 81% as x increases from 0 to 0.06 and then sharply falls to 52% as x further increases to 1 (Fig. 1(c)). The color

and brightness of Hf$_{1-x}$Ta$_x$N films gradually change following the regular evolution in λ_{Rmin} and R_{IR}, which is shown in Fig. 1(g). These results indicate that incorporation of Ta in the HfN film can effectively control the optical reflectivity.

To investigate the reason for reflectivity evolution via incorporation of Ta, the reflectance spectra of Hf$_{1-x}$Ta$_x$N films have been fitted through the Drude–Lorentz model, in which a series of spectral fittings have been carried out. The fitting parameters and their definitions are shown in Table I. The best fitting is obtained through using one Drude part and two Lorentz oscillators in the fitting process. The two oscillators located at $\sim$5.4 eV and $\sim$1.8 eV are defined as the high-energy (H) and low-energy (L) oscillators, respectively. The shape and peak position of the measured reflectivity spectra match well with the corresponding fitted spectra (Fig. S1 of the supplementary material), indicating that the reflectance spectra of Hf$_{1-x}$Ta$_x$N films can be fitted with the Drude-Lorentz model. The strong dependence between the fitting parameters and x is also displayed in Figs. 3(a) and S2 (supplementary material). The good agreement between the fitted reflectivity spectra and the measured ones proves that the observed variation in λ_{Rmin} and R_{IR} with x arises from the evolution in Lorentz and Drude parameters.

To look for the main contributing factors affecting λ_{Rmin} and R_{IR}, we have systematically studied the effect of Lorentz and Drude parameters on the reflectivity spectra through simulating the reflectivity spectra at different parameters (Figs. S3 and S4 of the supplementary material). As is seen from Fig. S3 (supplementary material), most Lorentz parameters have almost no influence on λ_{Rmin}, including the strength S_H (Fig. S3(e) of the supplementary material), the width Γ_H (Fig. S3(f) of the supplementary material), and the central energy E_H (Fig. S3(g) of the supplementary material) of the high-energy oscillator, and the width Γ_L (Fig. S3(i) of the supplementary material) and the central energy E_L (Fig. S3(j) of the supplementary material) in the low-energy oscillator. Additionally, the dielectric constant ε_∞ (Fig. S3(b) of the supplementary material) and relaxation time τ (Fig. S3(c) of the supplementary material) cause the consistent increase in λ_{Rmin}, which is totally different from the trend of measured λ_{Rmin} (Fig. 1(b)). Therefore, the variations in the parameters above are not the reason that λ_{Rmin} continuously decreases with x. In contrast, the increase in both plasma energy (E_p) and strength (S_L) of low-energy oscillator causes the marked reduction in λ_{Rmin} (Figs. 1(e) and 1(h)), which agrees well with the trend of the measured λ_{Rmin} (Fig. 1(b)). Therefore, the sharp blue-shift in λ_{Rmin} observed experimentally is due to the increase in E_p and S_L with x (Figs. 1(e) and 1(h)).

In Fig. S4 (supplementary material), all of Lorentz parameters (Figs. S4(e)–S4(j) of the supplementary material) and ε_∞ (Fig. S4(b) of the supplementary material) have almost no effect on R_{IR}, proving that these parameters do not contribute the changes in R_{IR}. In contrast, the increase in E_p causes a rapid rise in R_{IR}, whereas the reduction in τ causes a sharp fall in R_{IR}, indicating that E_p and τ are the main factors affecting R_{IR} (Figs. 1(f) and 1(i)). Therefore, the rise in the measured R_{IR} at $0 \le x \le 0.06$ is ascribed to the enhancement induced by E_p being greater than the fall induced by τ. As a result, the subsequent fall in the measured R_{IR} at $0.06 \le x \le 1$
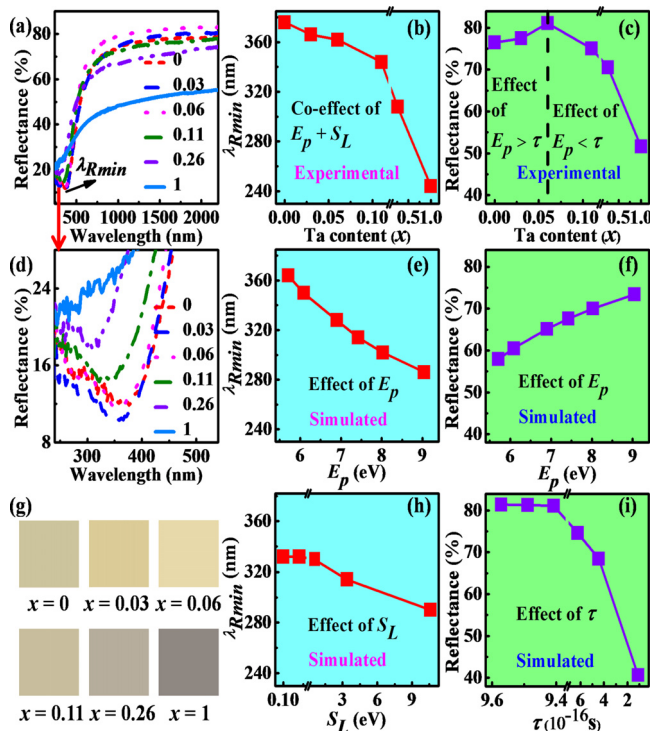

FIG. 1. The (a) reflectance spectra, (b) measured cutoff wavelengths at the minimum reflectance (λ_{Rmin}), (c) measured reflectance in the infrared region of 1000–2200 nm (R_{IR}), (d) a zoomed-in view of the region λ_{Rmin}, and (g) color variation for Hf$_{1-x}$Ta$_x$N films with different x. The simulated λ_{Rmin} obtained at different (e) plasma energy E_p and (h) strength S_L in the low-energy (O$_L$) Lorentz oscillator, and the simulated R_{IR} obtained at different (f) E_p and (i) relaxation time τ for the same samples.

232102-3   Gu *et al.*

Appl. Phys. Lett. **109**, 232102 (2016)

TABLE I. Drude-Lorentz parameters for the $Hf_{1-x}Ta_xN$ films with different x extracted from the fitting procedure: dielectric constant ε_∞, plasma energy E_p, relaxation time τ, central energy E_H, strength S_H, and width Γ_H in the high-energy oscillator, and central energy E_L, strength S_L, and width Γ_L in the low-energy oscillator.

Ta/(Hf + Ta) x	ε_∞	E_p (eV)	τ (10^{-16} s)	E_H (eV)	S_H (eV)	Γ_H (eV)	E_L (eV)	S_L (eV)	Γ_L (eV)
0.00	2.50	5.71	9.57	4.60	1.20	2.65	…	…	…
0.03	2.74	6.09	9.49	4.85	1.33	2.80	1.80	0.10	1.50
0.06	3.33	6.90	9.41	4.95	1.40	2.46	1.81	0.12	1.65
0.11	3.38	7.42	6.24	5.10	1.38	2.30	1.81	0.53	2.10
0.26	3.57	8.03	4.45	5.20	1.20	2.30	1.82	3.39	2.60
1.00	4.00	9.04	1.11	6.12	1.40	2.70	1.85	10.61	3.20

owes to the positive effect of E_p being less than the negative effect of τ.

In summary, the simulations of reflectivity spectra above prove that the decrease in λ_{Rmin} arises from the combined effect of E_p and S_L. The first increase and then decrease in R_{IR} are attributed to the competition between the positive and negative roles of E_p and τ.

To explain the reason that incorporation of Ta significantly affects the E_p, S_L, and τ, we have investigated the structure and electronic properties of $Hf_{1-x}Ta_xN$ films. Figs. 2(a) and 2(b) plot the GIXRD and symmetric $\theta/2\theta$ XRD spectra for δ-$Hf_{1-x}Ta_xN$ with different x. It can be seen that the (1 1 1), (2 0 0), (2 2 0), and (3 1 1) diffraction peaks attributed to the rocksalt phase appear simultaneously, proving that $Hf_{1-x}Ta_xN$ films keep crystallized in the rocksalt structure as x varies from 0 to 1. The lattice parameter (a) values experimentally obtained from GIXRD spectra and theoretically obtained by first-principles calculations are shown in Fig. 2(c). The measured a decreases consistently as x increases from 0 to 1, which agrees well with the trend of theoretical a, confirming that the incorporation of Ta causes a lattice contraction. These results consistently prove that incorporation of Ta in HfN films forms the solid solutions as x increases from 0 to 1. To confirm further this conclusion, Raman spectra, SAED, and HRTEM measurements were performed and the

corresponding results are displayed in Figs. 2(d)–2(f), respectively. The first-order acoustic (TA, LA) and optical peaks (O) at 110, 150 and 470 cm^{-1} assigned to the rocksalt structure appear simultaneously in Fig. 2(d) as x varies from 0 to 1. Fig. 2(e) displays the diffraction rings attributed to (1 1 1), (2 0 0), (2 2 0), and (3 1 1) in the rocksalt phase. Fig. 2(f) plots a typical HRTEM lattice image of $Hf_{1-x}Ta_xN$ films, in which. well-crystallized nanograins are uniformly distributed on the film surface. The measured interplanar spacings agree well with the (111) and (200) plane spacings of the rocksalt phase. These findings from Raman, SAED, and HRTEM match well with XRD measurements and first-principles calculations, consistently proving that incorporation of Ta in HfN films
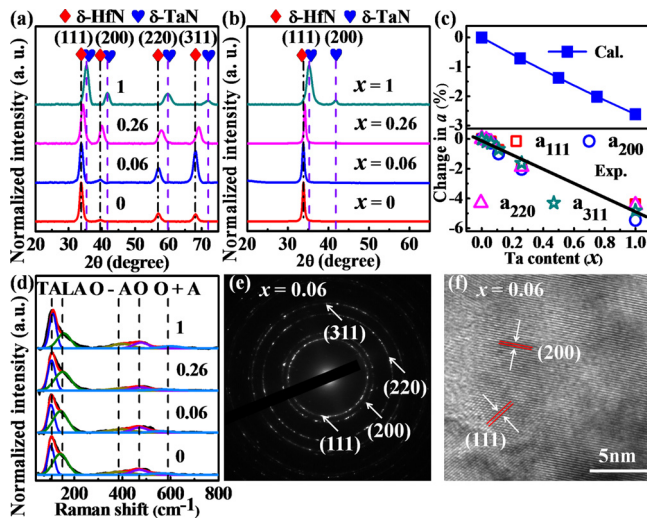

FIG. 2. The (a) GIXRD, (b) symmetric $\theta/2\theta$ XRD spectra, (c) change in lattice parameter experimentally obtained from GIXRD spectra and theoretically obtained by first-principles calculations, and (d) Raman spectra for δ-$Hf_{1-x}Ta_xN$ films with different x. A typical (e) SAED pattern and (f) HRTEM lattice image.
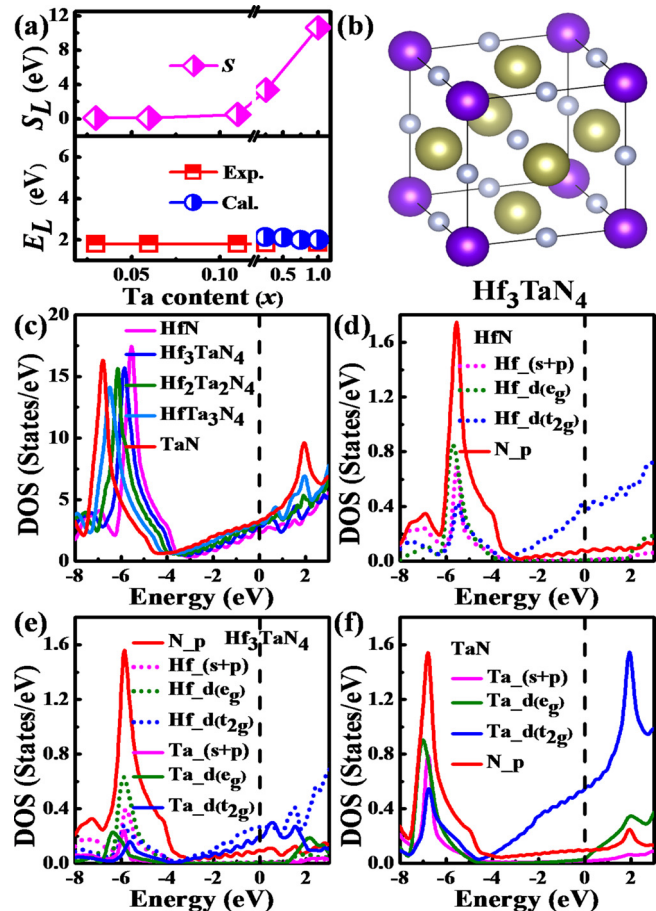

FIG. 3. The (a) central energy E_L and strength S_L in the low-energy Lorentz oscillator for $Hf_{1-x}Ta_xN$ films with different x. A (b) typical structural model and (c-f) density of states (DOS) for HfN, Hf_3TaN_4, $Hf_2Ta_2N_4$, $HfTa_3N_4$, and TaN obtained by first-principles calculations.

RIGHTSLINK

induces formation of $Hf_{1-x}Ta_xN$ solid solutions within the whole region of x from 0 to 1.

Now that the formation of $Hf_{1-x}Ta_xN$ solid solutions is confirmed, we explain the origin of the two unknown oscillators and change in strength (S_L) of the low-energy oscillator in Figs. 3(a) and S2 (supplementary material). The effect of Ta incorporation on the electronic structure is investigated by a combination of first-principles calculations and experiments. For better comparison with the experiments, five theoretical models of $Hf_{1-x}Ta_xN$ solid solutions are constructed, and the corresponding structure is plotted in Figs. 3(b) and S5 (supplementary material). The order in the structure is: $HfN \rightarrow Hf_3TaN_4 \rightarrow Hf_2Ta_2N_4 \rightarrow HfTa_3N_4 \rightarrow TaN$. The total and partial density of states (TDOS and PDOS) for HfN, Hf_3TaN_4, $Hf_2Ta_2N_4$, $HfTa_3N_4$, and TaN are calculated, and the corresponding results are shown in Figs. 3(c)–3(f). For pure HfN (Fig. 3(d)), the density of states (DOS) is mainly divided into three distinct energy regions. The first region from −8 to −3 eV is characterized by the strong hybridization of the Hf d-electrons with N p-electrons. The second region from −3 eV to Fermi level (E_F) is mainly from the t_{2g} electrons of Hf d. The third region from E_F to 3 eV is filled by the Hf d-t_{2g} electrons. For pure TaN (Fig. 3(f)), new e_g states at ∼2.0 eV above E_F occur and coexist with the t_{2g} electrons in the third region. In addition, for Hf_3TaN_4 solid solutions (Fig. 3(e)), the e_g states at ∼2.0 eV above E_F also appear in the third region. These results consistently prove that incorporation of Ta induces splitting of the d band above the E_F compared to the pure HfN, which results in the formation of e_g states at ∼2.0 eV above the E_F. In this situation, electrons trapped in t_{2g} occupied states close to the E_F can jump toward these e_g unoccupied states above the E_F, causing the transition absorption in the considered energy range. Therefore, the unknown absorption band centered at ∼1.80 eV corresponding to the lower-energy oscillator (Fig. 3(a)) can be attributed to the transitions from the t_{2g} occupied states to e_g unoccupied states due to crystal field splitting (calculated energy separation is ∼2.0 eV). The absorption band centered at ∼5.4 eV corresponding to the high-energy oscillator (Fig. S2(a) of the supplementary material) can be assigned to the intrinsic inter-band transition from the N2p electrons to the Fermi level (calculated energy separation is ∼6.1 eV). As x increases, $t_{2g} \rightarrow e_g$ absorption band gets stronger (Fig. 3(a)) because e_g unoccupied states above E_F become stronger (Figs. 3(e) and 3(f)).

Fig. 4(a) plots the plasma energy (E_p) and relaxation time (τ) as a function of x. As x increases from 0 to 1, E_p increases consistently from 5.71 eV to 9.04 eV, and τ decreases monotonically from 9.57×10^{-16} s to 1.11×10^{-16} s. According to the formula $E_p \propto n^{1/2}$, E_p is determined by the concentration of free electrons (n). Our hall measurements show that the n sharply increases from 2.47×10^{22} to 7.66×10^{22} cm^{-3} as x increases (Fig. 4(b)). This matches well with the trend of E_p (Fig. 4(a)), indicating that the increase in E_p is due to the increase in n after incorporation of Ta. Why does τ decrease as x increases (Fig. 4(a))? τ is the average time between two scattering events of free electrons, which is directly related to the electron mean free path (le). The increase in n causes increase in scattering events of electron-electron and electron-defect (point defects and grain boundaries), which in turn inevitably reduces the le.[41] Hence, the observed reduction in
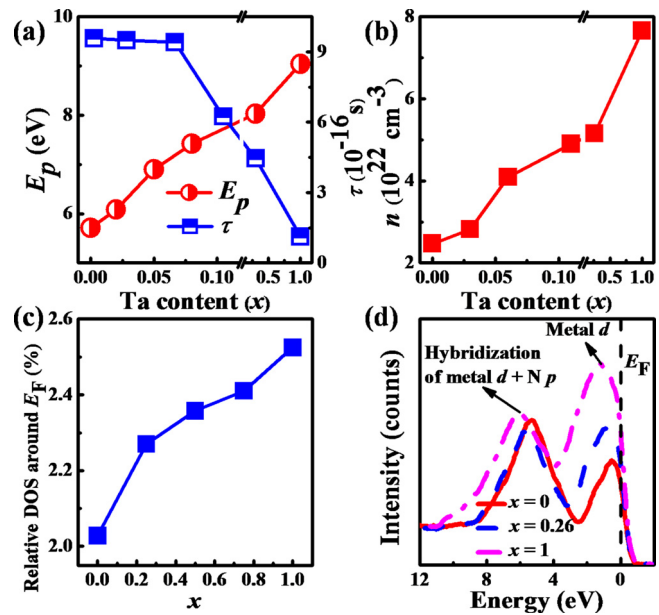

FIG. 4. The (a) plasma energy E_p and relaxation time τ, (b) concentration of free electrons n, the (c) ratio of the integrated DOS from −0.15 up to 0.15 eV to that of the whole valence energy region up to E_F obtained by first-principles calculations, and (d) typical valence-band spectra for $Hf_{1-x}Ta_xN$ films with different x.

τ is attributed to the increase in n. These results consistently prove that both increase in E_p and decrease in τ are due to the increase in n induced by Ta alloying.

To explain why the n continuously increases as x increases, the density of states (DOS) around the E_F for five δ-$Hf_{1-x}TaN_x$ samples mentioned above (Fig. 3(c)) is investigated. Fig. 4(c) plots the ratio of the integrated DOS from −0.15 up to 0.15 eV to that of the whole valence energy region up to E_F. It can be clearly seen that as x increases from 0 to 1, the DOS around E_F increases from 2.0% to 2.5%, indicating that incorporation of Ta adds extra free electrons to the conduction band. To confirm further this conclusion, the XPS valence-band spectra measurements were performed (Fig. 4(f)). All of the spectra are composed of two peaks. One is located around the E_F (0–3 eV), originating from metal d (Hf $4d$ and/or Ta $5d$) states based on calculated DOS (Figs. 3(d)–3(f)). The other peak is located at ∼5.5 eV from hybridized states of N $2p$ and metal d. The metal d states get stronger as x increases (Fig. 4(d)), which is consistent with the calculated DOS (Fig. 4(c)), indicating that Ta alloying adds extra free electrons to the conduction band because Ta (d^3s^2) has one more valence electron than Hf (d^2s^2).

As x increases from 0 to 0.26, hardness (H) and modulus (M) of $Hf_{1-x}Ta_xN$ films gradually increase up to 31.6 GPa and 320.0 GPa (Fig. S6 of the supplementary material). Compared to pure HfN (H = 24.3 GPa, M = 287.5 GPa) and TaN (H = 24.0 GPa, M = 289.5 GPa) films, the hardness of the $Hf_{1-x}Ta_xN$ film with x = 0.26 increases by 30% and 32%, and the modulus increases by 11% and 11%, respectively. The H and E improvement arises from the solid-solution hardening.[7]

In conclusion, incorporation of tantalum in the hafnium nitride film induces a tunable optical reflectivity and improves the hardness. The consistency between our experimental

results and first-principles calculations unambiguously proves that the increase in infrared reflectance is attributed to the increase in concentration of free electrons (n) because Ta (d^3s^2) has one more valence electron than Hf (d^2s^2). The sharp blue-shift in cutoff wavelength arises from the increase in n and formation of $t_{2g} \rightarrow e_g$ absorption band. These results suggest that alloying is an effective way to simultaneously improve the optical and mechanical properties of transition metal nitrides films, which provides a research strategy for preparing durable high-reflectance coatings used on the outer surface of optical devices in harsh environment.

See supplementary material for Figures S1–S6.

[1]G. Greczynski, S. Mráz, L. Hultman, and J. M. Schneider, Appl. Phys. Lett. **108**, 041603 (2016).

[2]H. An, Y. Kanno, T. Tashiro, Y. Nakamura, J. Shi, and K. Ando, Appl. Phys. Lett. **108**, 121602 (2016).

[3]J. A. Briggs, G. V. Naik, T. A. Petach, B. K. Baum, D. Goldhaber-Gordon, and J. A. Dionne, Appl. Phys. Lett. **108**, 051110 (2016).

[4]H. Z. Zhang, D. S. Ang, K. S. Yew, and X. P. Wang, Appl. Phys. Lett. **108**, 083505 (2016).

[5]A. A. Herzing, U. Guler, X. Zhou, A. Boltasseva, V. Shalaev, and T. B. Norris, Appl. Phys. Lett. **108**, 171107 (2016).

[6]I. L. Farrell, R. J. Reeves, A. R. H. Preston, B. M. Ludbrook, J. E. Downes, B. J. Ruck, and S. M. Durbin, Appl. Phys. Lett. **96**, 071914 (2010).

[7]G. Abadias, M. B. Kanoun, S. Goumri-Said, L. Koutsokeras, S. N. Dub, and P. Djemia, Phys. Rev. B **90**, 144107 (2014).

[8]C. Q. Hu, X. B. Zhang, Z. Q. Gu, H. H. Huang, S. Zhang, X. F. Fan, W. Zhang, Q. Wei, and W. T. Zheng, Scr. Mater. **108**, 141 (2015).

[9]L. Tsetseris, N. Kalfagiannis, S. Logothetidis, and S. T. Pantelides, Phys. Rev. Lett. **99**, 125503 (2007).

[10]L. Tsetseris, N. Kalfagiannis, S. Logothetidis, and S. T. Pantelides, Phys. Rev. B **76**, 224107 (2007).

[11]F. Rivadulla, M. Banobre-Lopez, C. X. Quintela, A. Pineiro, V. Pardo, D. Baldomir, M. A. Lopez-Quintela, J. Rivas, C. A. Ramos, H. Salva, J.-S. Zhou, and J. B. Goodenough, Nat. Mater. **8**, 947 (2009).

[12]C. X. Quintela, F. Rivadulla, and J. Rivas, Phys. Rev. B **82**, 245201 (2010).

[13]B. Alling, P. Steneteg, C. Tholander, F. Tasnádi, I. Petrov, J. E. Greene, and L. Hultman, Phys. Rev. B **85**, 245422 (2012).

[14]Z. Gu, C. Hu, H. Huang, S. Zhang, X. Fan, X. Wang, and W. Zheng, Acta Mater. **90**, 59 (2015).

[15]B. Alling, L. Hultberg, L. Hultman, and I. A. Abrikosov, Appl. Phys. Lett. **102**, 031910 (2013).

[16]B. Alling, A. V. Ruban, A. Karimi, L. Hultman, and I. A. Abrikosov, Phys. Rev. B **83**, 104203 (2011).

[17]C. X. Quintela, B. Rodríguez-González, and F. Rivadulla, Appl. Phys. Lett. **104**, 022103 (2014).

[18]L. E. Koutsokeras, G. Abadias, C. E. Lekka, G. M. Matenoglou, D. F. Anagnostopoulos, G. A. Evangelakis, and P. Patsalas, Appl. Phys. Lett. **93**, 011904 (2008).

[19]L. Tsetseris, S. Logothetidis, and S. T. Pantelides, Appl. Phys. Lett. **94**, 161903 (2009).

[20]B. Alling, C. Höglund, R. Hall-Wilton, and L. Hultman, Appl. Phys. Lett. **98**, 241911 (2011).

[21]C. Zhao, T. K. Ng, N. Wei, A. Prabaswara, M. S. Alias, B. Janjua, C. Shen, and B. S. Ooi, Nano Lett. **16**, 1056 (2016).

[22]S. Mahieu, W. P. Leroy, K. Van Aeken, M. Wolter, J. Colaux, S. Lucas, G. Abadias, P. Matthys, and D. Depla, Sol. Energy **85**, 538 (2011).

[23]G. Abadias, V. I. Ivashchenko, L. Belliard, and P. Djemia, Acta Mater. **60**, 5601 (2012).

[24]G. B. Smith, P. D. Swift, and A. Bendavid, Appl. Phys. Lett. **75**, 630 (1999).

[25]E. Budke, J. Krempel-Hesse, H. Maidhof, and H. Schüssler, Surf. Coat. Technol. **112**, 108 (1999).

[26]B. Alling, Phys. Rev. B **89**, 085112 (2014).

[27]L. Tsetseris, N. Kalfagiannis, S. Logothetidis, and S. T. Pantelides, Phys. Rev. B **78**, 094111 (2008).

[28]C.-G. Ribbing and A. Roos, *Optical Thin Films V: New Developments* (International Society for Optics and Photonics, 1997), pp. 148–162.

[29]W. Li, U. Guler, N. Kinsey, G. V. Naik, A. Boltasseva, J. Guan, V. M. Shalaev, and A. V. Kildishev, Adv. Mater. **26**, 7921 (2014).

[30]F. Nita, C. Mastail, and G. Abadias, Phys. Rev. B **93**, 064107 (2016).

[31]J. Kim, S.-H. Jhi, and K. Ryeol Lee, J. Appl. Phys. **110**, 083501 (2011).

[32]D. Valerini, M. A. Signore, A. Rizzo, and L. Tapfer, J. Appl. Phys. **108**, 083536 (2010).

[33]C. Q. Hu, Z. Q. Gu, J. B. Wang, K. Zhang, X. B. Zhang, M. M. Li, S. Zhang, X. F. Fan, and W. T. Zheng, J. Phys. Chem. C **118**, 20511 (2014).

[34]M. Strømme, R. Karmhag, and C. G. Ribbing, Opt. Mater. **4**, 629 (1995).

[35]H. Gueddaoui, G. Schmerber, M. Abes, M. Guemmaz, and J. C. Parlebas, Catal. Today **113**, 270 (2006).

[36]W. D. Sproul, D. J. Christie, and D. C. Carter, Thin Solid Films **491**, 1 (2005).

[37]W. D. Sproul, Thin Solid Films **107**, 141 (1983).

[38]W. D. Sproul, J. Vac. Sci. Technol., A **4**, 2874 (1986).

[39]W. D. Sproul, Thin Solid Films **118**, 279 (1984).

[40]Z. Q. Gu, C. Q. Hu, X. F. Fan, L. Xu, M. Wen, Q. N. Meng, L. Zhao, X. L. Zheng, and W. T. Zheng, Acta Mater. **81**, 315 (2014).

[41]J. L. Farvacque and Z. Bougrioua, Phys. Rev. B **68**, 035335 (2003).